

# Shape-Controlled Nanoparticles in Pore-Confined Space

Johannes Knossalla,<sup>‡,¶,||</sup> Paul Paciok,<sup>§,¶</sup> Daniel Göhl,<sup>†</sup> Daniel Jalalpoor,<sup>‡</sup> Enrico Pizzutilo,<sup>†,||</sup> Andrea M. Mingers,<sup>†</sup> Marc Heggen,<sup>§</sup> Rafal E. Dunin-Borkowski,<sup>§</sup> Karl J. J. Mayrhofer,<sup>†,||,⊥</sup> Ferdi Schüth,<sup>\*,‡</sup> and Marc Ledendecker<sup>\*,†,||</sup>

<sup>†</sup>Department of Interface Chemistry and Surface Engineering, Max-Planck-Institut für Eisenforschung GmbH, Max-Planck-Strasse 1, 40237 Düsseldorf, Germany

<sup>‡</sup>Department of Heterogeneous Catalysis, Max-Planck-Institut für Kohlenforschung, Kaiser-Wilhelm-Platz 1, 45470 Mülheim an der Ruhr, Germany

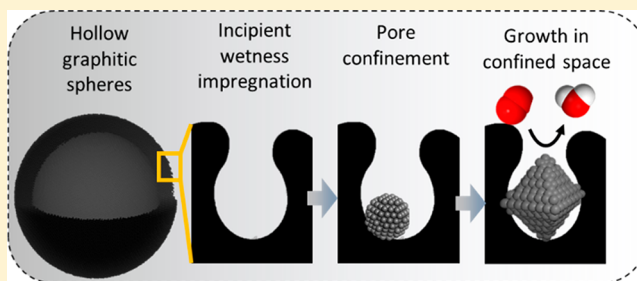
<sup>§</sup>Ernst-Ruska Centre for Microscopy and Spectroscopy with Electrons and Peter Grünberg Institute, Forschungszentrum Jülich, 52425 Jülich, Germany

<sup>¶</sup>Forschungszentrum Jülich GmbH, Helmholtz Institute Erlangen-Nürnberg for Renewable Energy (IEK-11), Egerlandstr. 3, 91058 Erlangen, Germany

<sup>⊥</sup>Department of Chemical and Biological Engineering, Friedrich-Alexander-Universität Erlangen-Nürnberg, Egerlandstr. 3, 91058 Erlangen, Germany

## Supporting Information

**ABSTRACT:** Increasing the catalyst's stability and activity are one of the main quests in catalysis. Tailoring crystal surfaces to a specific reaction has demonstrated to be a very effective way in increasing the catalyst's specific activity. Shape controlled nanoparticles with specific crystal facets are usually grown kinetically and are highly susceptible to morphological changes during the reaction due to agglomeration, metal dissolution, or Ostwald ripening. A strong interaction of the catalytic material to the support is thus crucial for successful stabilization. Taken both points into account, a general catalyst design is proposed, combining the enhanced activity of shape-controlled nanoparticles with a pore-confinement approach for high stability. Hollow graphitic spheres with narrow and uniform bimodal mesopores serve as model system and were used as support material. As catalyst, different kinds of particles, such as pure platinum (Pt), platinum/nickel (Pt<sub>3</sub>Ni) and Pt<sub>3</sub>Ni doped with molybdenum (Pt<sub>3</sub>Ni–Mo), have exemplarily been synthesized. The advantages, limits and challenges of the proposed concept are discussed and elaborated by means of time-resolved, *in* and *ex situ* measurements. It will be shown that during catalysis, the potential boundaries are crucial especially for the proposed catalyst design, resulting in either retention of the initial activity or drastic loss in shape, size and elemental composition. The synthesis and catalyst design can be adapted to a wide range of catalytic reactions where stabilization of shape-controlled particles is a focus.



## INTRODUCTION

The primary goals in catalysis are high activity, selectivity and stability in the target reaction while keeping the material and production costs low. In the last decades, the understanding of fundamental catalytic processes on an atomic level has led to substantial improvement in catalyst design. Among other factors, control of the shape and surface composition of catalyst nanoparticles has demonstrated its importance for different industrially relevant reactions.<sup>1–5</sup> For the oxygen reduction reaction, octahedral geometries with a high degree of {111} surfaces of face centered cubic (fcc) transition metals and metal alloys were identified as key driver for a high activity, combining high specific with high mass activity.<sup>6,7</sup> Despite their superior activity, their structure is highly susceptible to morphology and structural changes, a problem exacerbated by

a shortage of fundamental insights of how these degradation processes occur.<sup>6,8</sup> Besides the dissolution of non-noble metals and the accompanying surface restructuring, also structural changes on a higher level, such as particle detachment or agglomeration play an important role for the catalyst's stability. To achieve long-term stability, a homogeneous distribution and strong interaction of the catalytic material to the support is crucial. When taking it one step further, catalyst incorporation into pores of three-dimensional support materials actively suppresses detachment and agglomeration of neighboring nanoparticles—a particle pore confinement approach.<sup>9–17</sup> For successful pore confinement, particles of similar size range are

Received: July 24, 2018

Published: October 19, 2018

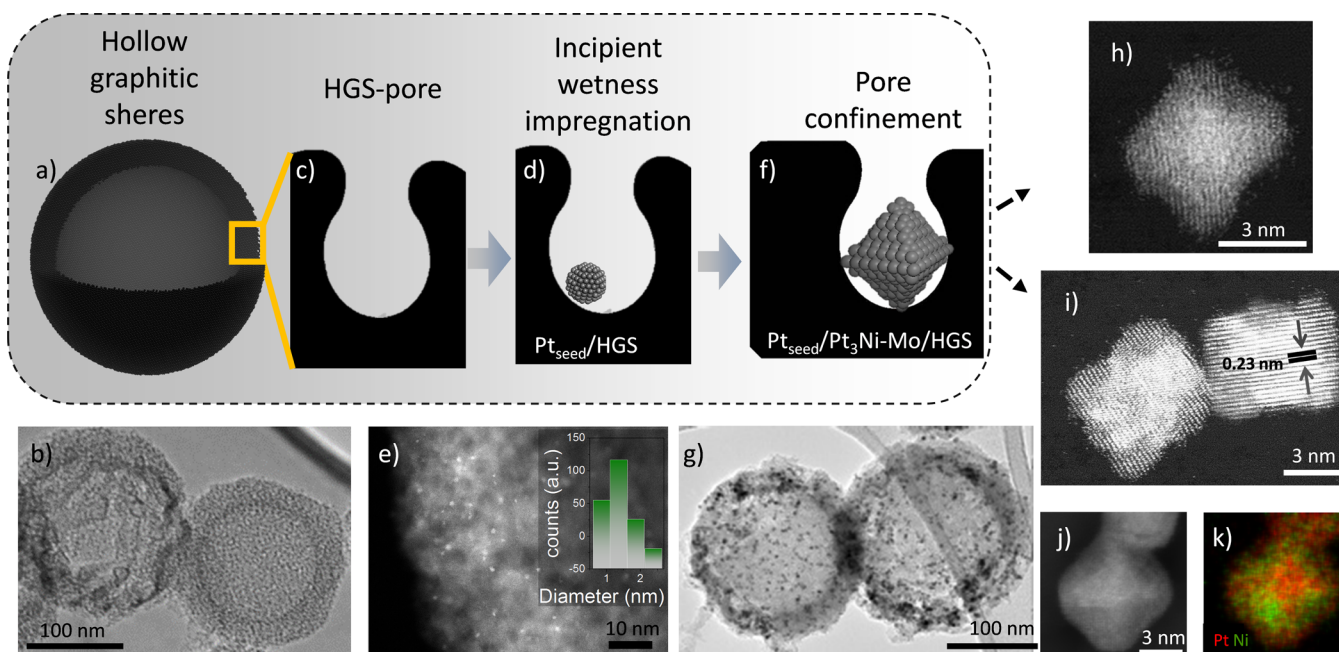


**Figure 1.** Schematic representation of the incorporation of octahedral  $\text{Pt}_3\text{Ni}(-\text{Mo})$  nanoparticles in the mesopores (c) of hollow graphitic spheres (a, b). The corresponding TEM micrographs are shown below. First, platinum seed particles are grown inside the mesopores (d, e) followed by the overgrowth of  $\text{Pt}_3\text{Ni}(-\text{Mo})$  octahedra (g). e, inset) Particle size distribution of  $\text{Pt}_{\text{seed}}/\text{HGS}$ . Selected octahedrally shaped particles after the incorporation into HGS (h, i) and the comparison on Vulcan (j, k) in dark field STEM mode.

encapsulated inside the pores, preventing particle movement on the support. Shape-controlled materials, however, are usually obtained via colloidal routes with capping agents such as polymers, ionic species or biomolecules that bind to specific facets and alter thereby their specific surface energy.<sup>18–20</sup> Despite the relative ease of colloidal synthesis routes, the nucleation and growth of shape-controlled particles, which are stabilized by capping agents, in confined space is a challenge yet to be solved. In this manuscript, a general synthetic procedure is proposed that combines the advantage of shape-controlled nanoparticles with a pore-confinement approach. It is demonstrated how to incorporate and position particle with octahedral geometries into pores with sizes in the same range as the particles themselves and that capping agents are able to direct crystal growth along a certain axis, even if the growth proceeds in confined space. This will be exemplarily demonstrated for different kinds of particles, including pure platinum (Pt), platinum/nickel ( $\text{Pt}_3\text{Ni}$ ) and  $\text{Pt}_3\text{Ni}$  doped with molybdenum ( $\text{Pt}_3\text{Ni}-\text{Mo}$ ). A focus will be placed on synthetic challenges, the advantages of the described catalyst design, limitations encountered during catalysis as well as the pivotal role of the support material.

## RESULTS AND DISCUSSION

Hollow graphitic spheres (HGS) serve as a model pore system for the study of particle incorporation into its bottleneck pores.<sup>21</sup> The HGS material combines high surface area (around 1000–1200  $\text{m}^2/\text{g}$ ) and a pore volume of 1.0–1.3  $\text{cm}^3 \text{g}^{-1}$  with a high degree of graphitization, resulting in lower carbon corrosion at high potentials compared to traditional carbon supports.<sup>22</sup> Hard templating offers the advantage of adjusting the pore size distribution (PSD) in a highly controlled manner with high reproducibility. The PSD of the materials used here, as determined by nitrogen sorption (Figure 2a), centers between 3 and 4 nm. As reference carbon

support, Vulcan XC-72R with high surface area was used, allowing for sufficient nucleation sites, so that a uniform dispersion of the octahedral catalyst particles should be feasible. The most active reported octahedral-shaped catalyst toward the ORR is based on  $\text{Pt}_3\text{Ni}$  doped with Mo, and the synthesis conditions were adapted from Huang and co-workers.<sup>23</sup> First, octahedral  $\text{Pt}_3\text{Ni}(-\text{Mo})$  particles were synthesized solvothermally in the presence of carbon support (HGS/Vulcan). DMF was used as a reducing agent and solvent. Benzoic acid, together with DMF, serves as a directing agent, which binds preferentially to  $\{111\}$  facets, resulting in octahedrons enclosed by  $\{111\}$  facets (c.f. experimental details in SI).<sup>23–25</sup> For Vulcan, the described synthesis route works well, yielding octahedral-shaped nanoparticle in the size range of  $6.4 \pm 1.4$  nm (longest axis) as shown in Figure S1 for  $\text{Pt}_3\text{Ni}$  and in Figure S3 for  $\text{Pt}_3\text{Ni}-\text{Mo}$ . The particles are larger than the mesopores of the HGS support, and on first glance, particle encapsulation in the 3–4 nm pores of HGS appeared to be difficult. Using the same synthesis conditions with the HGS material, the homogeneous nucleation of seed crystals and the selective growth along a certain axis takes predominantly place on the exterior of the hollow spheres and not inside the pores (Figures S5 and S6). The octahedral particles, along with preagglomerated particles, are inhomogeneously distributed over the HGS surface, because the conditions of particle encapsulation and the accompanying separation are not fulfilled. The main challenge was thus not the selective growth along a certain axis inside the pores, but rather suppressing homogeneous nucleation occurring inside and outside of the pores. To overcome this restriction, the synthesis was extended to a seed-mediated growth, as schematically shown in Figure 1. A preceding incipient wetness impregnation to induce nucleation was combined with a separated growth process, enabling a high dispersion under less stringent reaction conditions. The first nucleation is restricted to occur inside

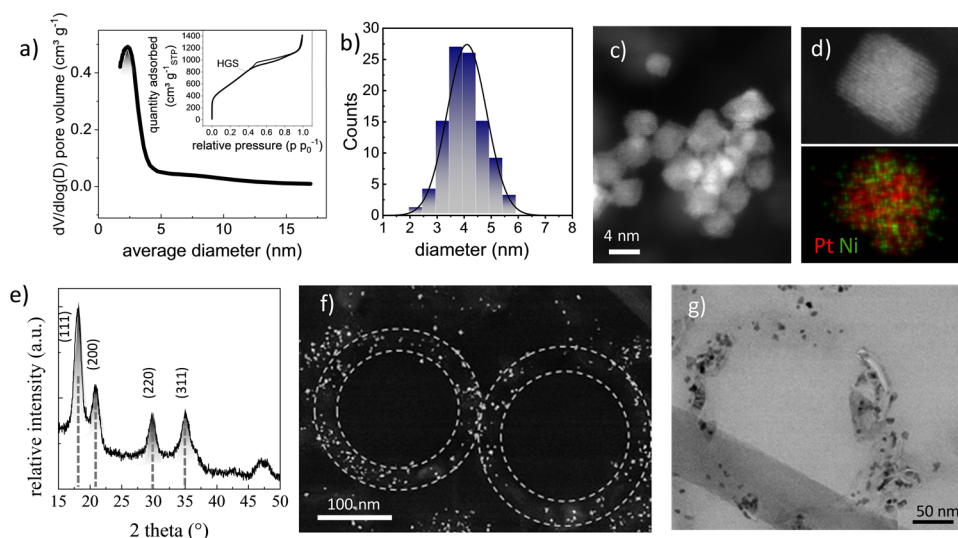


**Figure 2.** Nitrogen sorption of HGS (a) and the corresponding pore size distribution (inset).  $\text{Pt}_{\text{seed}}/\text{Pt}_3\text{Ni}$  octahedral particles (c) and the corresponding particle size distribution (b). X-ray diffractogram of individual  $\text{Pt}_{\text{seed}}/\text{Pt}_3\text{Ni}/\text{HGS}$  particles (gray dashed lines indicate the Pt reference [ICDD: 04-0802]) (e) and the corresponding high angle annular dark field (HAADF) scanning transmission electron microscopy (STEM) energy dispersive X-ray (EDX) images. STEM micrographs in dark (f) and bright (g) field mode of a cross-sectional microtome sliced full sphere of  $\text{Pt}_{\text{seed}}/\text{Pt}_3\text{Ni}/\text{HGS}$ . The dashed lines (f) symbolize the mesoporous carbon shell of the HGS support.

the HGS pores, and Pt-seeds with a diameter of  $1.3 \pm 0.3$  nm are incorporated in the mesopores of the HGS ( $\text{Pt}_{\text{seed}}/\text{HGS}$ , Figure 1d,e, Figure S7) acting as anchor points for the subsequent overgrowth process. The corresponding particle size distribution of the seed particles is shown in Figure 1e. Subsequently, a solvothermal overgrowth process using benzoic acid and DMF as surfactant and solvent yielded nanoparticles with an edge length of  $4.1 \pm 0.7$  nm (from STEM micrographs, denoted as  $\text{Pt}_{\text{seed}}/\text{Pt}_3\text{Ni}(-\text{Mo})/\text{HGS}$ , Figure 2b,c; Figures S8, S9 and S10). The longest axis is much smaller compared to  $\text{Pt}_3\text{Ni}$  supported on Vulcan, indicating growth limitation induced by the mesopores of the HGS. Elemental maps of representative  $\text{Pt}_3\text{Ni}-\text{Mo}/\text{C}$  octahedra show an inhomogeneous elemental distribution indicating a segregation of Ni at the {111} planes (Figure 1j,k, Figure S4). As intended, the overgrowth process enables the formation of finely dispersed octahedral particles with only infrequently remaining spherical particles (Figures 1g and 2c,f,g). In a survey of 200 particles, 75% of  $\text{Pt}_{\text{seed}}/\text{Pt}_3\text{Ni}-\text{Mo}/\text{HGS}$  were identified to be octahedra with minor imperfections like rounded corners or concave surfaces, which is a common observation.<sup>26,27</sup>

The heterogeneous nucleation and followed growth on already existing, in HGS embedded Pt-seed particles is kinetically favored over the homogeneously occurring nucleation of Pt at the outside of HGS. The separation of nucleation and growth favors a uniform morphology and narrow particle size distribution as shown in Figure 2b,c. X-ray diffraction displays the characteristic reflections of platinum with the respective (111), (200), (220) and (311) planes (dashed lines,  $\text{Pt}_{\text{seed}}/\text{Pt}_3\text{Ni}/\text{HGS}$ , Figure 2e;  $\text{Pt}_{\text{seed}}/\text{Pt}_3\text{Ni}-\text{Mo}/\text{HGS}$ , Figure S11). The reflection shift to higher diffraction angles agrees with Vegard's law, resulting from the incorporation of smaller Ni/Mo-atoms in the fcc Pt structure. The EDX map of a representative  $\text{Pt}_{\text{seed}}/\text{Pt}_3\text{Ni}-\text{Mo}/\text{HGS}$  particle demonstrates a homogeneous elemental distribution of platinum and nickel (Figure 2d). Only a negligible number of agglomerated particles are observed by (S)TEM, which may

serve as first evidence for the successful incorporation of alloyed particles into the pores (Figure 1g). In order to inspect the location of the particles with respect to the HGS surface, cross-sectional specimens were prepared by embedding HGS into epoxy resin and by sectioning it into 30 nm thick slices using a microtome. The cross-sectional micrographs ( $\text{Pt}_{\text{seed}}/\text{Pt}_3\text{Ni}/\text{HGS}$ : Figure 2f,g;  $\text{Pt}_{\text{seed}}/\text{Pt}_3\text{Ni}-\text{Mo}/\text{HGS}$ : Figure S8) confirm that particles are formed predominantly within the mesoporous shell of the HGS support. In order to evaluate whether the specific shape of the catalyst particles grown in the confining pores translates to improved performance, the catalysts were tested for the ORR in acidic medium. The activity of  $\text{Pt}_{\text{seed}}/\text{Pt}_3\text{Ni}(-\text{Mo})$  was analyzed in an *ex situ* rotating disk electrode (RDE) setup in 0.1 M  $\text{HClO}_4$ . In Figure 3, the activity trends of  $\text{Pt}_3\text{Ni}-\text{Mo}$  on Vulcan and  $\text{Pt}_{\text{seed}}/\text{Pt}_3\text{Ni}-\text{Mo}$  on HGS are summarized. As expected,  $\text{Pt}_{\text{seed}}/\text{Pt}_3\text{Ni}-\text{Mo}/\text{HGS}$  ( $1.23 \pm 0.14$  mA/cm<sup>2</sup><sub>Pt</sub>) outperforms the reference Pt catalyst (Pt/C,  $0.47 \pm 0.07$  mA/cm<sup>2</sup><sub>Pt</sub>) in specific activity (Figure 3). The electrochemically active surface area (ECSA) of  $\text{Pt}_{\text{seed}}/\text{Pt}_3\text{Ni}-\text{Mo}/\text{HGS}$  is higher compared to  $\text{Pt}_3\text{Ni}-\text{Mo}/\text{C}$ , which is attributed to the smaller

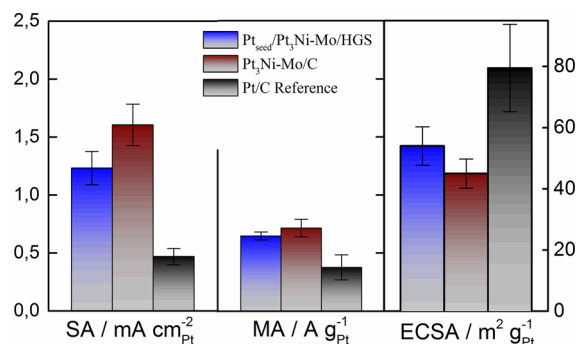


**Figure 3.** Specific and mass activity of  $\text{Pt}_{\text{seed}}/\text{Pt}_3\text{Ni}-\text{Mo}$  on HGS and Vulcan at 0.9  $V_{\text{RHE}}$  and the corresponding electrochemically active surface area determined via CO-stripping. Pt/C was chosen as reference (TKK, 3 nm).

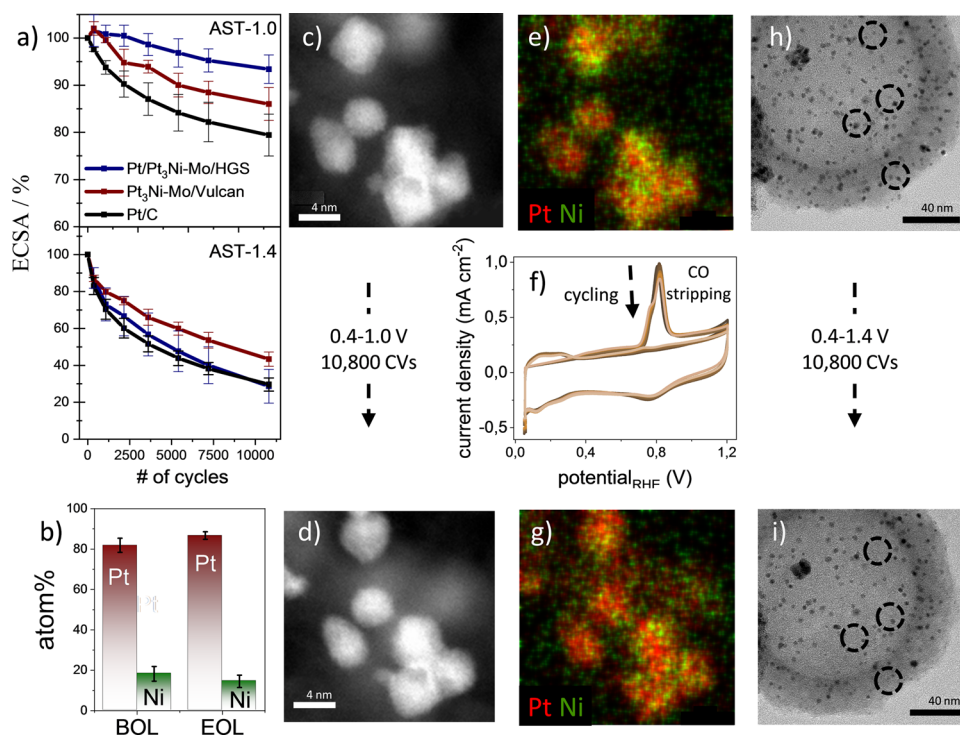


**Figure 4.** Stability of shape-controlled nanoparticles on different supports. (a) ECSA development over 10 800 cycles between 0.4 and 1.0 V/1.4 V (AST-1.0 and AST-1.4). IL-STEM and EDX images of Pt<sub>seed</sub>/Pt<sub>3</sub>Ni-Mo/HGS before (BOL, c, e) and after AST-1.0 (EOL, d, g) and the compositional change (from EDX) of single octahedrons determined from nine different locations (b). (f) CO stripping after 0, 360, 1080, 2160, 3600, 5400, 7200 and 10800 potential cycles (dark to bright) between 0.4 and 1.0 V. IL-STEM images of Pt<sub>seed</sub>/Pt<sub>3</sub>Ni-Mo/HGS. IL-TEM images of Pt<sub>seed</sub>/Pt<sub>3</sub>Ni-Mo/HGS before (h) and after AST-1.4 (i).

particle dimensions observed from STEM. When comparing CO-stripping and  $H_{UPD}$  for surface area determination, the adsorption/desorption of hydrogen on Pt<sub>seed</sub>/Pt<sub>3</sub>Ni-Mo was suppressed substantially compared to Pt/C. This is in line with literature and has been assigned to a downshift of the d-band center position for Pt<sub>3</sub>Ni(111) compared to Pt(111) surface terminations (Figure S17).<sup>1</sup> The smaller octahedron size results in a lower specific activity and can be attributed to the higher oxophilicity and the resulting stronger binding to oxygen intermediates to the surface. For pristine Pt nanoparticles (NP), the specific activity (SA) increases with increasing particle diameter: Pt (1–5 nm) < Pt black particles (around 30 nm) < polycrystalline Pt indicating a particle size dependency on the activity.<sup>28</sup> Because the synthesis allows growth of octahedra in the smallest size dimensions reported, a similar conclusion might be drawn. Another reason might be the Pt-core in the octahedra interior, which reduces the total amount of Ni, with an overall negative impact on the SA. The higher ECSA (smaller NP size) and lower SA results in a similar mass activity (MA) of (Pt<sub>seed</sub>/)Pt<sub>3</sub>Ni-Mo on HGS compared to Vulcan.

The relevant {111} facets seem to be largely utilized under the applied conditions, and electrolyte accessibility does not seem to be negatively affected.

Besides the observed increased activity, it is expected that the proposed design results in higher stability over many thousands of degradation cycles due to pore confinement. However, the evaluation of a catalyst's stability is challenging and depends strongly on the applied reaction conditions. *Ex situ* potential cycling between 0.4 V vs RHE and different upper potential limits gives a first estimation of the catalyst stability. The two upper potential limits represent (i) fuel cell

operating conditions or open circuit potentials in air (1.0 V<sub>RHE</sub>) and (ii) higher potential perturbations due to, e.g., fuel cell start-up (1.4 V<sub>RHE</sub>).<sup>29,30</sup> For Pt–Ni based octahedra, Strasser and co-workers found, first, an increase in ECSA when cycled up to 1.0 V, followed by further dealloying and formation of a Pt-rich surface. Especially high Pt to Ni ratios were reported to be beneficial for increased stability.<sup>24,25</sup> A similar trend was observed when performing accelerated stress tests (AST) between 0.4 to 1.0 V vs RHE (AST-1.0) in 0.1 M HClO<sub>4</sub> as shown in Figure 4a and Figure S12. First, the ECSA increases, attributed to the formation of a protecting Pt-layer, and declines afterward slightly. After 10 800 cycles, over 90% of the initial ECSA is retained for the pore confined particles. Because the in HGS incorporated NPs have substantially smaller particle dimensions compared to those reported in literature (and on Vulcan), which typically results in lower stability, a significant change in ECSA was expected. The opposite holds true, and the smaller, encapsulated octahedra are more stable and almost retain their initial ECSA. Up to 1.0 V, the low decline of ECSA for Pt<sub>seed</sub>/Pt<sub>3</sub>Ni-Mo/HGS is attributed to particle stabilization in the confined space. This is also confirmed by identical location scanning transmission electron microscopy (IL-STEM) measurements before and after potential cycling (Figure 4c,d,e,g, S14). In order to quantify the change in particle morphology and the concomitant loss of the 111 surface, particles in or close to the 110 zone axis were analyzed regarding the total height/length of the octahedral particles (Figure S18). After AST-1.0, 90% of the octahedra aligned in the 110 zone axis keep their octahedral morphology. The observed particles aligned in 110 zone axis showed some deterioration of the low coordinated and high energetic edge sites resulting in the formation of

truncated octahedra with an average particle contraction of 15%. Based on a simple model, the octahedra contraction leads to a 111 surface loss of 9%. We assigned these changes to Ni-, Mo- and (to some extent) Pt-dissolution as discussed further on. A detailed analysis can be found in the SI. IL-STEM experiments on the Pt<sub>3</sub>Ni–Mo/C material reveal the dissolution of nickel and an enrichment of platinum on the octahedra surface after 10,800 cycles, leading to the increased stability of the octahedral particles (Figure S4). A similar stabilization mechanism is assumed for Pt<sub>seed</sub>/Pt<sub>3</sub>Ni–Mo/HGS. Based on the elemental maps for the cycled Pt<sub>seed</sub>/Pt<sub>3</sub>Ni–Mo octahedra, however, a formation of a platinum-rich shell can be neither confirmed nor ruled out. As expected, particles enclosed in the pore system do not coalesce due to the enhanced interparticle distance and shielding by the pore walls (Figure S12). Agglomeration/detachment of the particles on the external graphitic domains probably contribute mostly to the observed drop in ECSA (keeping over 90% of the original ECSA after 10 800 cycles), because for these particles, the protecting pores are not effective. While potential cycling to upper potential limits of 1.0 V reveals higher stabilization of shape-controlled particles incorporated in the HGS mesopores, cycling to 1.4 V results in a drastic drop in ECSA of more than 50% for all shape-controlled nanoparticles. IL-STEM after ATP-1.4 reveals drastic changes in particle geometries resulting in spherical nanoparticles (Figures S2 and S15). The average particle size decreases and goes along with complete vanishing of individual particles as shown in Figure 4h,i and Figure S15). We attribute these changes to an almost quantitative dissolution of Ni and Mo and partial dissolution of Pt, as shown by time-resolved electrocatalytic flow cell measurements coupled to an inductively coupled plasma mass spectrometer (FC-ICP-MS, Figure 5). These measurements allow the identification of the underlying, fundamental degradation processes by monitoring the metal dissolution in situ, while the applied potential is swept and the current monitored.<sup>29</sup> In line with previous results on Pt-dissolution, Pt dissolves transiently when it is oxidized and reduced.<sup>31,32</sup> For the oxide formation process, potentials higher than ca. 1.0 V are necessary, explaining the retained high ECSA values from RDE experiments for AST-1.0. Mo-doping was reported to increase the stability by reducing the overall metal dissolution due to the local preference of Mo to surface vertex and edge sites.<sup>23</sup> This effect, however, could not be observed in our experiments, neither on the HGS nor on the Vulcan supported catalysts. Almost all Mo dissolves when brought into contact with the electrolyte. The remaining Mo dissolves almost quantitatively at low potentials (<1.0 V) leaving Pt and Ni behind. The almost quantitative dissolution might be an indication of the reported preference of Mo to occupy vertex/edge sites.<sup>23</sup> If not stabilized, Mo oxidizes in several stages as discussed in more detail in the SI.<sup>33</sup> Even though Ni dissolves as well, after stabilization of a Pt-rich surface, the surface seems to be stable up to 1.0 V, which is in line with previous IL-STEM/EDX results (Figure 4b,c,d,e,g).

Potentials sweeps up to 1.4 V, however, force Pt to be oxidized and reduced, with the accompanying dissolution of the noble metal. Nickel is highly susceptible to these oxidation state changes, forcing the octahedral morphology to collapse as shown by IL-STEM before and after catalysis (Figure 4h,i, Figure S15). As mentioned, the observed dissolution is responsible for particle shrinkage, and the correspondingly facilitated movement out of the pores results in final particle

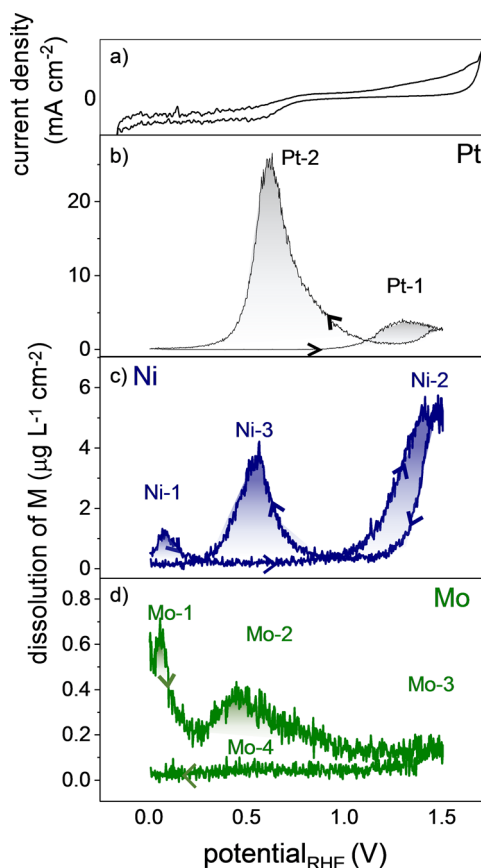


**Figure 5.** (a) *In situ*, potential- and time-dependent flow cell measurements coupled to an ICP-MS of Pt<sub>seed</sub>/Pt<sub>3</sub>Ni–Mo/HGS cycling the potential from 0 to 1.5 V<sub>RHE</sub> in 0.1 M HClO<sub>4</sub>. The current voltage curves are displayed in panel a while the potential dependent dissolution of Pt (b), Ni (c) and Mo (d) is shown below. The corresponding dissolution peaks are indicated, quantified and explained in detail in the SI.

detachment and the observed drop in ECSA (Figure S12). A detailed analysis and quantification of the dissolution processes and peak allocation can be found in the SI (Figure S13). These results indicate the importance of the potential boundary conditions for the proposed catalyst design that should be adhered to, especially for a potential use in real applications.

## CONCLUSION

A general adaptable synthesis strategy is proposed, which is suitable to position and grow shape-controlled nanoparticles with a high degree of (111) facets in defined mesopores. Pt<sub>seed</sub> particles obtained via incipient wetness impregnation ensure a homogeneous particle distribution. The subsequent overgrowth process in the presence of shape directing agents results in octahedra that are in the same size range as the pores themselves, and much smaller compared to octahedra synthesized on Vulcan. The smaller particle dimension in HGS leads to a higher ECSA, a lower SA and a similar MA compared to octahedra on Vulcan. The combination of IL-STEM, RDE testing and FC-ICP-MS measurements allowed the analysis of potential dependent morphological, structural and compositional changes due to dissolution, agglomeration and detachment. We demonstrate the advantages of shape-controlled particles confined in pores and their limitations. Especially the applied reaction conditions that effect shape-

controlled nanoparticles have direct consequences for the proposed strategy. The proposed design appears to be adaptable to a wide range of catalytic reactions and opens new possibilities for the synthesis of active and stable catalysts.

## ■ ASSOCIATED CONTENT

### Supporting Information

The Supporting Information is available free of charge on the ACS Publications website at DOI: 10.1021/jacs.8b07868.

Detailed description of the experimental details, material characterization and additional catalytic results (PDF)

## ■ AUTHOR INFORMATION

### Corresponding Authors

\*schueth@kofo.mpg.de

\*m.ledendecker@mpie.de

### ORCID

Johannes Knossalla: 0000-0002-2220-6670

Enrico Pizzutilo: 0000-0003-2733-7407

Marc Ledendecker: 0000-0003-3740-401X

### Author Contributions

<sup>†</sup>These authors contributed equally.

### Notes

The authors declare no competing financial interest.

## ■ ACKNOWLEDGMENTS

E.P and D.J. acknowledge financial support from the IMPRS-SurMat doctoral program. In addition, we thank Ann-Christin Swertz and Norbert Pfänder for their help with the microtome sectioning and STEM, and C. Weidenthaler is gratefully acknowledged for the support in the XRD measurements. This research has been funded by the Federal Ministry for Economic Affairs and Energy (BMWf) of Germany in the framework of PtTM@HGS (project number 03ET6080A).

## ■ REFERENCES

- (1) Stamenkovic, V. R.; Fowler, B.; Mun, B. S.; Wang, G.; Ross, P. N.; Lucas, C. A.; Marković, N. M. *Science* **2007**, *315*, 493.
- (2) Chen, C.; Kang, Y.; Huo, Z.; Zhu, Z.; Huang, W.; Xin, H. L.; Snyder, J. D.; Li, D.; Herron, J. A.; Mavrikakis, M.; Chi, M.; More, K. L.; Li, Y.; Markovic, N. M.; Somorjai, G. A.; Yang, P.; Stamenkovic, V. R. *Science* **2014**, *343*, 1339.
- (3) Marković, N. M.; Ross, P. N. *Surf. Sci. Rep.* **2002**, *45*, 117.
- (4) Burda, C.; Chen, X.; Narayanan, R.; El-Sayed, M. A. *Chem. Rev.* **2005**, *105*, 1025.
- (5) Ledendecker, M.; Schlott, H.; Antonietti, M.; Meyer, B.; Shalom, M. *Adv. Energy Mater.* **2017**, *7*, 1601735.
- (6) Beermann, V.; Gocyla, M.; Willinger, E.; Rudi, S.; Heggen, M.; Dunin-Borkowski, R. E.; Willinger, M.-G.; Strasser, P. *Nano Lett.* **2016**, *16*, 1719.
- (7) Strasser, P. *Science* **2015**, *349*, 379.
- (8) Komanicky, V.; Chang, K.-C.; Menzel, A.; You, H.; Wang, X.; Myers, D.; Markovic, N. *ECS Trans.* **2005**, *1*, 167.
- (9) Mezzavilla, S.; Baldizzone, C.; Swertz, A.-C.; Hodnik, N.; Pizzutilo, E.; Polymeros, G.; Keeley, G. P.; Knossalla, J.; Heggen, M.; Mayrhofer, K. J. J.; Schüth, F. *ACS Catal.* **2016**, *6*, 8058.
- (10) Baldizzone, C.; Mezzavilla, S.; Carvalho, H. W. P.; Meier, J. C.; Schuppert, A. K.; Heggen, M.; Galeano, C.; Grunwaldt, J.-D.; Schüth, F.; Mayrhofer, K. J. *Angew. Chem., Int. Ed.* **2014**, *53*, 14250.
- (11) Galeano, C.; Meier, J. C.; Peinecke, V.; Bongard, H.; Katsounaros, I.; Topalov, A. A.; Lu, A.; Mayrhofer, K. J. J.; Schüth, F. *J. Am. Chem. Soc.* **2012**, *134*, 20457.

(12) Wang, G.; Xu, S.; Wang, L.; Liu, Z.; Dong, X.; Wang, L.; Zheng, A.; Meng, X.; Xiao, F.-S. *Chem. Commun.* **2018**, *54*, 3274.

(13) Zhang, J.; Wang, L.; Zhang, B.; Zhao, H.; Kolb, U.; Zhu, Y.; Liu, L.; Han, Y.; Wang, G.; Wang, C.; Su, D. S.; Gates, B. C.; Xiao, F.-S. *Nature Catalysis* **2018**, *1*, 540.

(14) Wang, G.-H.; Hilgert, J.; Richter, F. H.; Wang, F.; Bongard, H.-J.; Spliethoff, B.; Weidenthaler, C.; Schüth, F. *Nat. Mater.* **2014**, *13*, 293.

(15) Liu, J.; Wickramaratne, N. P.; Qiao, S. Z.; Jaroniec, M. *Nat. Mater.* **2015**, *14*, 763.

(16) Yang, T.; Ling, H.; Lamoniér, J.-F.; Jaroniec, M.; Huang, J.; Monteiro, M. J.; Liu, J. *NPG Asia Mater.* **2016**, *8*, e240.

(17) Tian, H.; Huang, F.; Zhu, Y.; Liu, S.; Han, Y.; Jaroniec, M.; Yang, Q.; Liu, H.; Lu, G. Q. M.; Liu, J. *Adv. Funct. Mater.* **2018**, *28*, 1870227.

(18) Ahmadi, T. S.; Wang, Z. L.; Green, T. C.; Henglein, A.; El-Sayed, M. A. *Science* **1996**, *272*, 1924.

(19) Sun, Y.; Xia, Y. *Science* **2002**, *298*, 2176.

(20) Xia, Y.; Xia, X.; Peng, H.-C. *J. Am. Chem. Soc.* **2015**, *137*, 7947.

(21) Galeano, C.; Meier, J. C.; Peinecke, V.; Bongard, H.; Katsounaros, I.; Topalov, A. A.; Lu, A. H.; Mayrhofer, K. J. J.; Schüth, F. *J. Am. Chem. Soc.* **2012**, *134*, 20457.

(22) Polymeros, G.; Baldizzone, C.; Geiger, S.; Grote, J. P.; Knossalla, J.; Mezzavilla, S.; Keeley, G. P.; Cherevko, S.; Zeradjanin, A. R.; Schüth, F.; Mayrhofer, K. J. *J. Electrochim. Acta* **2016**, *211*, 744.

(23) Huang, X.; Zhao, Z.; Cao, L.; Chen, Y.; Zhu, E.; Lin, Z.; Li, M.; Yan, A.; Zettl, A.; Wang, Y. M.; Duan, X.; Mueller, T.; Huang, Y. *Science* **2015**, *348*, 1230.

(24) Cui, C.; Gan, L.; Heggen, M.; Rudi, S.; Strasser, P. *Nat. Mater.* **2013**, *12*, 765.

(25) Cui, C.; Gan, L.; Li, H.-H.; Yu, S.-H.; Heggen, M.; Strasser, P. *Nano Lett.* **2012**, *12*, 5885.

(26) Huang, X.; Zhao, Z.; Chen, Y.; Zhu, E.; Li, M.; Duan, X.; Huang, Y. *Energy Environ. Sci.* **2014**, *7*, 2957.

(27) Choi, S.-I.; Xie, S.; Shao, M.; Odell, J. H.; Lu, N.; Peng, H.-C.; Protsailo, L.; Guerrero, S.; Park, J.; Xia, X.; Wang, J.; Kim, M. J.; Xia, Y. *Nano Lett.* **2013**, *13*, 3420.

(28) Nesselberger, M.; Ashton, S.; Meier, J. C.; Katsounaros, I.; Mayrhofer, K. J. J.; Arenz, M. *J. Am. Chem. Soc.* **2011**, *133*, 17428.

(29) Ohma, A.; Shinohara, K.; Iiyama, A.; Yoshida, T.; Daimaru, A. *ECS Trans.* **2011**, *41*, 775.

(30) Kocha, S. S. In *Polymer Electrolyte Fuel Cell Degradation*; Kumbur, E. C., Veziroglu, T. N., Eds.; Academic Press: Boston, 2012; p 89.

(31) Topalov, A. A.; Katsounaros, I.; Attinger, M.; Cherevko, S.; Meier, J. C.; Klemm, S. O.; Mayrhofer, K. J. *J. Angew. Chem., Int. Ed.* **2012**, *51*, 12613.

(32) Cherevko, S.; Keeley, G. P.; Geiger, S.; Zeradjanin, A. R.; Hodnik, N.; Kulyk, N.; Mayrhofer, K. J. *J. ChemElectroChem* **2015**, *2*, 1471.

(33) Ledendecker, M.; Mondschein, J. S.; Kasian, O.; Geiger, S.; Göhl, D.; Schalenbach, M.; Zeradjanin, A.; Cherevko, S.; Schaak, R. E.; Mayrhofer, K. *Angew. Chem., Int. Ed.* **2017**, *56*, 9767.